PAN POLSKA AKADEMIA NAUK

METROLOGY AND MEASUREMENT SYSTEMS

Index 330930, ISSN 0860-8229
www.metrology.pg.gda.pl

M&MS

SIDESLIP ANGLE ESTIMATION OF IN-WHEEL MOTOR DRIVE ELECTRIC VEHICLES BY CASCADED MULTI-KALMAN FILTERS AND MODIFIED TIRE MODEL

Long Chen, Te Chen, Xing Xu, Yingfeng Cai, Haobin Jiang, Xiaoqiang Sun

Jiangsu University, School of Automotive and Traffic Engineering, Zhenjiang 212013, China
(✉ *chenlong@ujs.edu.cn*, +86 511 8878 2845, *ujschente@163.com*, *xuxing@mail.ujs.edu.cn*, *caicaixiao0304@126.com*, *jianghb@ujs.edu.cn*, *sunxqujs@126.com*)

Abstract

Reliable estimation of longitudinal force and sideslip angle is essential for vehicle stability and active safety control. This paper presents a novel longitudinal force and sideslip angle estimation method for four-wheel independent-drive electric vehicles in which the cascaded multi-Kalman filters are applied. Also, a modified tire model is proposed to improve the accuracy and reliability of sideslip angle estimation. In the design of longitudinal force observer, considering that the longitudinal force is the unknown input of the electric driving wheel model, an expanded electric driving wheel model is presented and the longitudinal force is obtained by a strong tracking filter. Based on the longitudinal force observer, taking into consideration uncertain interferences of the vehicle dynamic model, a sideslip angle estimation method is designed using the robust Kalman filter and a novel modified tire model is proposed to correct the original tire model using the estimation results of longitudinal tire forces. Simulations and experiments were carried out, and effectiveness of the proposed estimation method was verified.

Keywords: distributed drive electric vehicle, Kalman filter, error compensation, sideslip angle.

1. Introduction

As a potential means of future transportation with accurate and independent torque manoeuvrability [1–5], the *four-wheel independent-drive electric vehicles* (4WID-EVs), a promising activation pattern of electric vehicles with higher freedom in vehicle dynamic control, have attracted the attention of both industrial and academic communities for the last decades. The stable performance of vehicle dynamics control depends on the precise and credible vehicle state measurements [6–10]. Recently, the increasing requirements and developing technologies on vehicle stability and active safety motivate the growth of intelligent transportation and autonomous vehicles. The auxiliary driving and self-driving, with an advantage of vehicle autonomous security and reduced mobility cost, has attracted the attention and considerate efforts of researchers and companies [11–14]. The estimation of longitudinal force and sideslip angle is also important to the vehicle path-following and lateral stability control. Considering the longitudinal force and sideslip angle are difficult and costly to be measured by the on-board vehicle sensors, the design of estimators for longitudinal force and sideslip angle estimation is essential.

Article history: received on Jun. 05, 2018; accepted on Oct. 30, 2018; available online on Mar. 29, 2019, DOI: 10.24425/mms.2019.126329.

The existing studies present different forms of observer designs for vehicle state estimation, and the algorithms used for observer design in prior papers can adopt a Kalman-filter-based method [15–19], a nonlinear-observer-based method [20–24], an optimal estimation method [25–29], an information fusion estimation method [17, 19, 29–33], a robust estimation method [34–37] *et al.* The Kalman filter is widely used in vehicle state estimation and recently, on the basis of characteristics of the objects to be estimated, researchers approach to designing the vehicle state estimators applying a fusion of Kalman filter with another advanced estimation theory. Nam proposed a novel sideslip angle estimation method using a combination of recursive least squares and Kalman filter, in which the recursive least squares was designed with assistance of a forgetting factor [21]. Liu presented a vehicle state estimation strategy on the basis of the extended Kalman filter and the minimum model error theory, where the minimum model error theory was used to reduce the estimation error caused by model nonlinearity [23]. In most prior approaches, the longitudinal force is usually estimated for a traditional internal-combustion-engine vehicle; the longitudinal force observer designs for EVs, especially for 4WID-EVs are still relatively difficult to encounter. In [37], the longitudinal force estimation was obtained by integrating the rotational dynamics differential equation of driving wheel or using the current multiplied by a constant. If we apply the measurements of current, speed, and voltage for the longitudinal force estimation, we can make full use of the electric driving characteristics of 4WID-EVs. Lots of vehicle dynamics control systems need to monitor the sideslip angle dynamically, so in a variety of works the sideslip angle estimation have been researched extensively. Due to the importance of sideslip angle, the design process of sideslip angle estimator is focused on the enhancement of estimation performance and accuracy. Ma analysed the transfer function frequency with the consideration of steering wheel torque and steering wheel angle and presented a novel steering torque-based sideslip angle estimation method [22]. Jin established a nonlinear vehicle dynamics model, a linear tire model and a nonlinear tire model, and then proposed an interacting multiple-model filter-based estimator, in which updating of the model probability was considered [24].

In this paper, a design of a novel *strong-tracking filter-based* (STF) *longitudinal force observer* (LFO) for 4WID-EVs is presented and – based on the LFO design – a sideslip angle estimation

Table 1. Terms and abbreviations.

Terms	**Abbreviations**
Four-wheel independent drive electric vehicles	4WID-EVs
Extended Kalman filter	EKF
Strong tracking filter	STF
Robust Kalman filter	RKF
Longitudinal force observer	LFO
Electric driving wheel model	EDWM
3-degree-of-freedom	3-DOF
Double Lane Changes	DLC
Rapid prototyping platform	RPP
Global position system	GPS
Inertial measurement unit	IMU
Root mean square	RMS
Root-mean-square error	E_{RMS}

method using the *robust Kalman filter* (RKF) is proposed. The vehicle dynamics model and *electric driving wheel model* (EDWM) are established. In the design of LFO, considering the EDWM is an uncertain system with unknown input, an extended model is presented and then the LFO is designed based on STF. On the basis of the designed LFO, considering the uncertainty of vehicle model, the RKF is studied and applied to the estimation of sideslip angle. Moreover, with the longitudinal forces being able to be obtained by LFO and the original tire model, the information redundancy of longitudinal forces was used to improve the accuracy and real-time tracking ability by error iteration. And the revised longitudinal force is further used to correct the lateral tire forces of the original tire model. The paper's main contribution includes: firstly, introducing the electric driving characteristic of 4WID-EV into the longitudinal force estimation by constructing the EDWM, secondly, using the multiple Kalman filters to design a sideslip angle observer and a modified tire model that help to improve the estimation accuracy and adaptability in multiple working conditions.

The terms and abbreviations used in this paper are listed in Table 1. The rest of this paper is organized as follows. The vehicle model is presented is Section 2. The design of vehicle state observers are included in Section 3. The simulation results are provided in Section 4. The experimental verifications are presented in Section 5, followed by the conclusive remarks.

2. Vehicle dynamics model

2.1. 3-degree-of-freedom vehicle model

A schematic diagram of the 3-DOF vehicle model in the longitudinal, lateral, and yaw directions is shown in Fig. 1. The origin of the dynamic coordinate system xoy fixed on the vehicle coincides with the vehicle gravity centre, the x axis is the longitudinal axis of the vehicle (the forward direction is positive), the y axis is the lateral axis of the vehicle (the right-to-left direction is positive). The pitch, roll, vertical motions and the suspension system of the vehicle are ignored. It is assumed that the mechanical properties of each tire are the same. The successive numbers 1, 2, 3, and 4 of the wheels correspond to the front-left, the front-right, the rear-left and the rear-right wheels, respectively. The dynamic equations of the 3-DOF vehicle model can be expressed as:

$$\dot{v}_x = \gamma v_y + \frac{1}{m}\left[(F_{x1} + F_{x2})\cos\delta - \left(F_{y1} + F_{y2}\right)\sin\delta + F_{x3} + F_{x4}\right], \tag{1}$$

$$\dot{v}_y = -\gamma v_x + \frac{1}{m}\left[(F_{x1} + F_{x2})\sin\delta + \left(F_{y1} + F_{y2}\right)\cos\delta + F_{y3} + F_{y4}\right], \tag{2}$$

$$\begin{aligned}\dot{\gamma} = \frac{1}{I_z}\big[&(F_{x1} + F_{x2})\,l_f\sin\delta - (F_{y3} + F_{y4})l_r + \left(F_{y1} + F_{y2}\right)l_f\cos\delta \\ &+ (F_{y1} - F_{y2})b_f\sin\delta - (F_{x1} - F_{x2})b_f\cos\delta - (F_{x3} - F_{x4})b_r\big],\end{aligned} \tag{3}$$

where v_x and v_y are the longitudinal and lateral vehicle speeds, respectively. γ is the yaw rate, m is the vehicle mass, δ represents the steering angle of the front wheels, I_z stands for the moment of inertia. F_{xj} and F_{yj} ($j = 1, 2, 3, 4$) are the longitudinal and lateral forces of the jth tire, respectively. l_f and l_r are the distances from the vehicle gravity centre to the front and rear axles, respectively. b_f and b_r are the half treads of the front wheels and rear wheels, respectively.

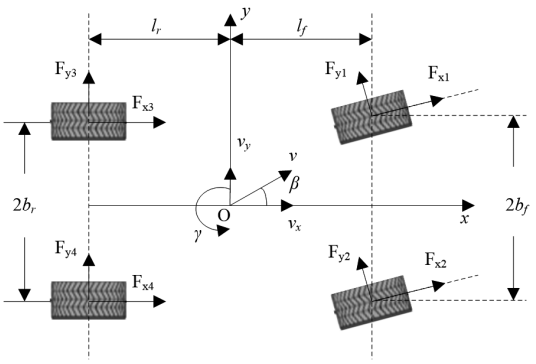

Fig. 1. A vehicle dynamics model.

2.2. Tire model

The following semi-empirical magic formula of tire model is used in order to estimate the longitudinal and lateral tire forces which can be computed as:

$$F_{x,y} = D\sin\{C\arctan[B\alpha - E(B\alpha - \arctan(B\alpha))]\}, \tag{4}$$

where B is the stiffness factor, C is the curve shape factor, D is the peak factor, E is the curve curvature factor, α is the wheel sideslip angle. The tire model parameters: B, C, D, E, are related to the tire vertical load. The vertical load of each tire can be calculated as:

$$\begin{cases} F_{z1} = l_r\left(\dfrac{mg}{2l} + \dfrac{ma_y h}{2b_f l}\right) - \dfrac{ma_x h}{2l} \\ F_{z2} = l_r\left(\dfrac{mg}{2l} - \dfrac{ma_y h}{2b_f l}\right) - \dfrac{ma_x h}{2l} \\ F_{z3} = l_f\left(\dfrac{mg}{2} + \dfrac{ma_y h}{2b_r l}\right) + \dfrac{ma_x h}{2l} \\ F_{z4} = l_f\left(\dfrac{mg}{2} - \dfrac{ma_y h}{2b_r l}\right) + \dfrac{ma_x h}{2l} \end{cases}, \tag{5}$$

where F_{z1}, F_{z2}, F_{z3}, and F_{z4} are the vertical loads of corresponding tires, h is the height of the centre of gravity, g is the acceleration of gravity. The sideslip angle of each wheel can be obtained by:

$$\begin{cases} \alpha_1 = \delta - \arctan\dfrac{v_y + l_f\gamma}{v_x + b_f\gamma/2} \\ \alpha_2 = \delta - \arctan\dfrac{v_y + l_f\gamma}{v_x - b_f\gamma/2} \\ \alpha_3 = -\arctan\dfrac{v_y - l_r\gamma}{v_x + b_r\gamma/2} \\ \alpha_4 = -\arctan\dfrac{v_y - l_r\gamma}{v_x - b_r\gamma/2} \end{cases}. \tag{6}$$

2.3. Electric-driven wheel model

A diagram of EDWM is shown in Fig. 2. The 4WID-EV is actuated by four in-wheel motors, and the electromechanical coupling driving wheel composed of a motor and a tire can be considered as an independent information module, so the concept of the EDMW is introduced to the longitudinal force estimation process and the current, speed and voltage are used to estimate the longitudinal force. The rotational dynamic equation of EDWM is as follows:

$$J_1\dot{\omega}_j = T_{Lj} - F_{xj}r, \tag{7}$$

where ω_j represents the rotational speed of the jth wheel, J_1 denotes the inertia moment, r represents the effective rolling radius of EDWM, T_{Lj} stands for the load torque of in-wheel motor. The balance equation of torque in the output shaft of EDWM is shown as:

$$J_2\dot{\omega}_j + b\omega_j = K_t i_j - T_{Lj}\,, \tag{8}$$

where J_2 is the rotational inertia of in-wheel motor rotor, b is the damping coefficient, K_t is the motor torque constant, i_j is the bus current. The dynamic voltage balance equation of equivalent circuit in in-wheel motor has the form:

$$u_j = Ri_j + L\dot{i_j} + K_a\omega_j\,. \tag{9}$$

where u_j is the bus voltage of in-wheel motor, R is the equivalent resistance of winding, L is the equivalent inductance of winding, K_a is the inverse electromotive force coefficient.

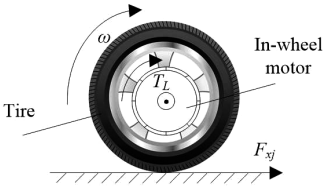

Fig. 2. A diagram of electric driving wheel model.

3. Observer design

3.1. Design of longitudinal force observer

By substituting (7) into (8) and combining it with (9), the EDWM is written as:

$$\begin{cases} \dot{i_j} = -\dfrac{R}{L}i_j - \dfrac{K_a}{L}\omega_j + \dfrac{1}{L}u_j \\ \dot{\omega}_j = \dfrac{K_t}{J}i_j - \dfrac{b}{J}\omega_j - \dfrac{r}{J}F_{xj} \end{cases}, \tag{10}$$

where $J = J_1 + J_2$. The EDWM in equation can be expressed as:

$$\begin{cases} \dot{x} = Ax + Bu + Dd + Ew_1 \\ y_w = Cx + Fw_2 \end{cases}, \tag{11}$$

where x, u, d and y are the state vector, the known input vector, the unknown input vector and the measurement vector, respectively. w_1 and w_2 are uncorrelated zero mean white noise sequences. The known input and unknown input represent the voltage and longitudinal force, respectively. And, $x = [i_j \omega_j]^T$, $A = \begin{bmatrix} -\frac{R}{L} & -\frac{K_a}{L} \\ \frac{K_t}{J} & -\frac{b}{J} \end{bmatrix}$, $B = \begin{bmatrix} \frac{1}{L} \\ 0 \end{bmatrix}$, $D = \begin{bmatrix} 0 \\ -\frac{r}{J} \end{bmatrix}$, $C = \begin{bmatrix} 1 & 0 \\ 0 & 1 \end{bmatrix}$, $E = F = \begin{bmatrix} 1 \\ 1 \end{bmatrix}$.

Compared with the common Kalman filter, the *strong-tracking filter* (STF) introduces the fading factor into the prediction error covariance matrix, so it has a stronger real-time tracking ability of system state. The nonlinear state space equation is defined as:

$$\begin{cases} \dot{x}(t) = f(x(t), u(t)) + \Gamma w(t) \\ y(t) = h(x(t), u(t)) + v(t) \end{cases}, \tag{12}$$

where $w(t)$ and $v(t)$ are the process noise and the measurement noise in accordance with Gauss distribution, respectively. The corresponding algorithm of STF is presented as follows:

1) Calculate the matrices of residual error and mean square error:

$$\begin{cases} r(k+1) = Y(k+1) - H(k+1)\hat{X}(k+1) \\ V_0(k+1) = \begin{cases} r(1)r^T(1), & k = 0 \\ \dfrac{\rho V_0(k) + r(k+1)r^T(k+1)}{\rho + 1}, & k \geq 1 \end{cases} \end{cases}, \tag{13}$$

where $0 \leq \rho \leq 1$ is the forgetting factor, choose $\rho = 0.95$.

2) Calculate the suboptimal fading factor:

$$\lambda(k+1) = \begin{cases} \lambda_0, & \lambda_0 \geq 1 \\ 1, & \lambda_0 \leq 1 \end{cases}, \tag{14}$$

where: $\begin{cases} \lambda_0 = \frac{\mathrm{tr}[N_{k+1}]}{\mathrm{tr}[M_{k+1}]} \\ N_{k+1} = V_{k+1} - H_{k+1}\Gamma_k Q_k \Gamma_k^T H_{k+1}^T - \beta R_{k+1} \\ M_{k+1} = H_{k+1}\Phi_{k+1/k} P_{k/k} \Phi_{k/k} H_{k+1}^T \end{cases}$. Here, $\beta \geq 1$ is the softening factor.

3) Calculate the matrices of prediction covariance matrix and gain:

$$\begin{cases} P_{k+1/k} = \lambda_{k+1}\Phi_{k+1/k} P_{k/k} \Phi_{k+1/k}^T + \Gamma_k Q_{k+1} \Gamma_k^T \\ K_{K+1} = P_{k+1/k} H_{k+1}^T [H_{k+1} P_{k+1/k} H_{k+1}^T + R_{K+1}]^{-1} \end{cases}. \tag{15}$$

4) Calculate the matrix of state estimation covariance and the estimation of state vector:

$$\begin{cases} P_{k+1/k+1} = (I - K_{k+1} H_{k+1}^T) P_{k+1/k} \\ \hat{X}_{k+1/k+1} = \hat{X}_{k+1/k} + K_{k+1} r_{k+1} \end{cases}. \tag{16}$$

The data flow chart of STF is shown in Fig. 3. Owing to the existence of unknown input in system (11), we construct the Markoff process as follows:

$$\begin{bmatrix} \dot{F}_{xj} \\ \ddot{F}_{xj} \end{bmatrix} = \begin{bmatrix} 0 & 1 \\ 0 & 0 \end{bmatrix} \begin{bmatrix} \dot{F}_{xj} \\ \ddot{F}_{xj} \end{bmatrix} + noise. \tag{17}$$

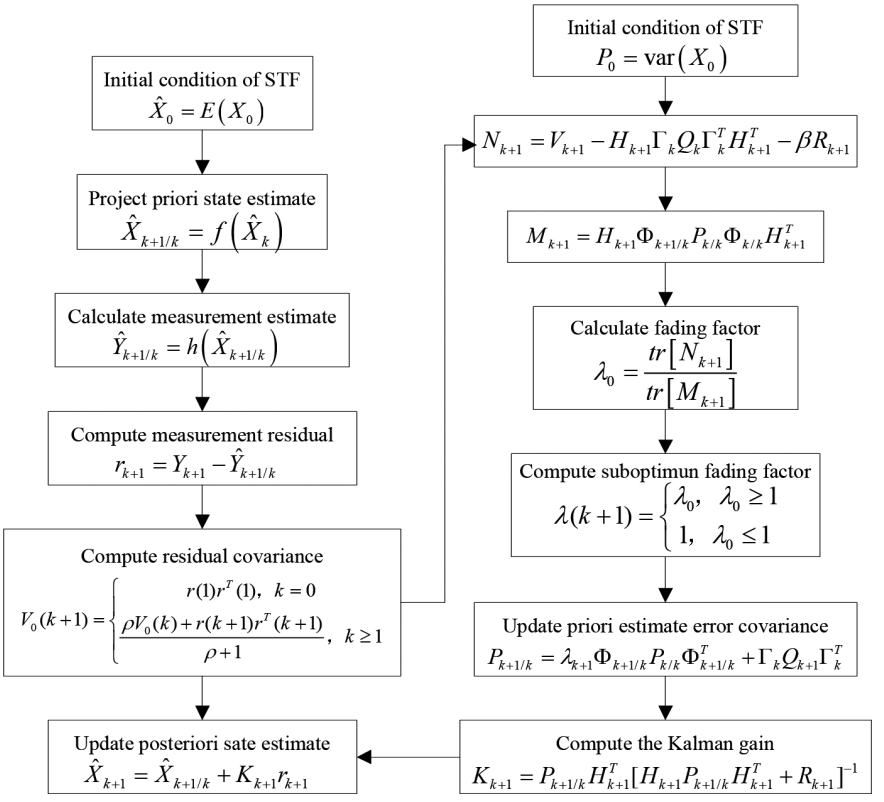

Fig. 3. A data flowchart of STF.

Expanding the system state by longitudinal force and its differential we obtain the expanded system state as $x_e = [i_j \;\; \omega_j \;\; F_{xj} \;\; \dot{F}_{xj}]^T = [x_{e1} \;\; x_{e2} \;\; x_{e3} \;\; x_{e4}]^T$. On the basis of the above mentioned STF, the estimator for longitudinal force estimation can be designed, the state space equation and the measurement equation of STF are expressed as follows, respectively.

$$\begin{cases} \dot{x}_{e1} = -\dfrac{R}{L}x_{e1} - \dfrac{K_a}{L}x_{e2} + \dfrac{1}{L}u \\ \dot{x}_{e2} = \dfrac{K_t}{J}x_{e1} - \dfrac{b}{J}x_{e3} - \dfrac{r}{J}x_{e3} \\ \dot{x}_{e3} = x_{e4} \\ \dot{x}_{e4} = 0 \end{cases}, \tag{18}$$

$$y_e = [i_j \;\; \omega_j]^T. \tag{19}$$

For a four-wheel independent-drive electric vehicle, each electric-driven wheel is an independent information unit. Therefore, we can respectively design four STFs corresponding to the four EDWMs, and the longitudinal forces can be estimated by the measurements of current, wheel speed and bus voltage, where STF1, STF2, STF3 and STF4 are applied to estimate F_{x1}, F_{x2}, F_{x3} and F_{x4}, respectively.

3.2. Sideslip angle estimation by cascaded multi-Kalman filters and modified tire model

Taking the unknown interferences into account, the vehicle states and parameters are time-varying in complex driving conditions. Under these circumstances, even small model errors will lead to the deviations of estimated values with the accumulation of time. In (1), (2), (3), considering the uncertainty of vehicle model, and assuming that the additional nonlinear factors are bounded, the discretization form of vehicle system model can be written as:

$$\begin{cases} x(k+1) = (A + \Delta A)\, x(k) + Bu(k) + Dw(k) \\ y(k) = (H + \Delta H)\, x(k) + v(k) \end{cases}, \tag{20}$$

where and represent the unknown disturbance of state transition matrix and measurement matrix caused by system uncertainty.

Defining the uncertainty as Δ and $\Delta < \Delta_0$, Δ, w and v are unrelated:

$$E(v) = E(w) = 0, \qquad \mathrm{var}(v) = R, \qquad \mathrm{var}(w) = P. \tag{21}$$

According to (21), it can be deduced that:

$$z = Hx + Hw + \Delta x + \Delta w + v. \tag{22}$$

According to (22), it can be found that:

$$\mathrm{var}(z) = \mathrm{var}(Hx) + \mathrm{var}(Hw) + \mathrm{var}(\Delta x) + \mathrm{var}(\Delta w) + \mathrm{var}(v), \tag{23}$$

where $\mathrm{var}(Hx)=0$, $\mathrm{var}(Hw)=HPH^T$, $\mathrm{var}(\Delta w)<\Delta_0 P\Delta_0^T$, $\mathrm{var}(\Delta x)<(|\Delta x|)\times(|\Delta x|)=x^T\left(\Delta_0^T\times\Delta_0^T\right)x$. Thus, it can be obtained that:

$$\sup \mathrm{var}(z) = HPH^T + x^T\left(\Delta_0^T \times \Delta_0^T\right) x + \Delta_0 P \Delta_0^T + R. \tag{24}$$

So, the rationality and feasibility of robust Kalman filter is satisfied. With regard to the system in (20), the steps of *robust Kalman filter* (RKF) can be presented as following.

1) The one-step prediction information of system status is:

$$x(k|k-1) = Ax(k-1). \tag{25}$$

The information matrix of $x(k)$ is:

$$\begin{aligned} &I\left[x(k|k-1)|x(k)\right]x(k|k-1) = P^{-1}(k|k-1) \\ &= \left[(A+\Delta_{A0})P(k-1)(A+\Delta_{A0})^T + x^T(k-1)\left(\Delta_{A0}^T \times \Delta_{A0}^T\right)x(k-1) + BQ(k-1)B^T\right]^{-1}. \end{aligned} \tag{26}$$

2) The information matrix of measurement $z(k)$ is expressed as:

$$I\left[z(k)|x(k)\right] = H^T\left[x^T(k-1)\left(\Delta_{H0}^T \times \Delta_{H0}^T\right)x(k-1) + R(k)\right]^{-1} H. \tag{27}$$

3) With the fusion of one-step prediction information and measurement of $x(k)$, the optimal estimation of $x(k)$ and its information matrix is given by:

$$\begin{aligned} x(k) = {} & P(k)\left\{P^{-1}(k|k-1)\right\}x(k|k-1) \\ & + H^T\left[x^T(k-1)\left(\Delta_{H0}^T \times \Delta_{H0}^T\right)x(k-1) + R(k)\right]^{-1} z(k)\}\text{no left bracket}, \end{aligned} \tag{28}$$

$$P^{-1}(k) = P^{-1}(k|k-1) + H^T\left[x^T(k-1)\left(\Delta_{H0}^T \times \Delta_{H0}^T\right)x(k-1) + R(k)\right]^{-1} H. \tag{29}$$

A data flowchart of robust Kalman filter is shown in Fig. 4.

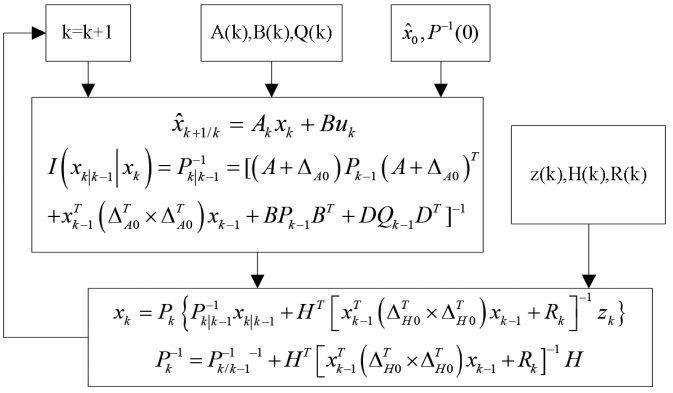

Fig. 4. A data flowchart of RKF.

In the process of RKF design, the longitudinal forces estimated by LFOs are regarded as the pseudo-measurements obtained by virtual sensors and used as inputs of robust Kalman filter. And the input variable is expressed as $u_k = [\delta \;\; F_{x1} \;\; F_{x2} \;\; F_{x3} \;\; F_{x4} \;\; F_{y1} \;\; F_{y2} \;\; F_{y3} \;\; F_{y4}]^T$, the state variable is given by $x_k = [v_x \;\; v_y \;\; \gamma]^T$, and the measurement is denoted as $y_k = [a_x \;\; a_y]^T$, where a_x and a_y represent the longitudinal acceleration and lateral acceleration of vehicle, respectively, and can be computed as:

$$\begin{cases} a_x = \dot{v}_x - \gamma v_y \\ a_y = \dot{v}_y + \gamma v_x \end{cases}. \tag{30}$$

In the RKF design, it is known that the lateral tire forces are obtained from the tire model. Moreover, the longitudinal forces also can be achieved from the tire model. So it can be noticed that the longitudinal force information has a redundancy considering the longitudinal forces estimated by LFOs, so we can utilize the redundancy of longitudinal forces to correct and compensate the tire model. The LFO is proposed on the basis of electromechanical coupling characteristics, so LFO is considered to have a quick response ability and a real-time tracking ability. The tire model is accurate but complex, so it can be used to obtain the longitudinal force estimation if the time delay can be ignored. That is to say, both tire model and the designed LFO have their advantage and applicability in longitudinal force estimation.

Here, for the convenience of expression, the longitudinal forces estimated by LFOs are denoted as F_{x1L}, F_{x2L}, F_{x3L}, F_{x4L}, the longitudinal forces computed by the tire model are denoted as F_{x1M}, F_{x2M}, F_{x3M}, F_{x4M}, the longitudinal forces computed by the modified tire model are denoted as F_{x1}, F_{x2}, F_{x3}, F_{x4}, the notation of lateral tire force is the same as that of longitudinal force. Through analysis, it can be found that the longitudinal force obtained by LFO indicates that the tire is in good contact with the road and the longitudinal slip of tire is non-existent. Therefore, if the longitudinal slip is obvious, the estimation accuracy of LFO will reduce. It is affirmative that the timely calculation ability of the tire model is weaker than that of LFO. That is to say, as for the real-time estimation ability, the vehicle speed is the most significant factor influencing the tire model; the larger vehicle speed is, the more obvious is the estimation error of the tire model.

The modified tire model is presented, in which a fuzzy controller is designed to coordinate the calculation results of LFOs and those of the tire model. The longitudinal slip rate of each tire can be calculated by $\lambda_j = \dfrac{\omega_j r - v_x}{v_x}$ $(j = 1, 2, 3, 4)$, so that the composite longitudinal tire slip

$\lambda_0 = |\lambda_1| + |\lambda_2| + |\lambda_3| + |\lambda_4|$ is used to characterize the slip degree of tire. In the fuzzy controller, the inputs are vehicle speed v_x and longitudinal tire slip λ_0, and the output is the fuzzy weight k_f used to balance LFO and the tire model, in which the v_x and λ_0 symbolize the confidence level of LFO and tire model, respectively. Thus, the optimal longitudinal force estimation of the modified tire model can be written as $F_{xj} = k_f F_{xjL} + (1 - k_f) F_{xjM}$. The membership functions of the inputs and output in the fuzzy controller are shown in Fig. 5, whereas the fuzzy control rules are listed in Table 2. With the dependable longitudinal force information, the error between F_{xj} and F_{xjM} can be applied to reflect the deviation from the original tire model and, furthermore, it can be used to correct the lateral tire forces of the original tire model. Therefore, based on the experience from the design principle of PID controller, the optimal lateral force of the modified tire model can be obtained by:

$$F_{yj} = F_{yjM} + k_P \left(F_{xj} - F_{xjM} \right) + k_I \int \left(F_{xj} - F_{xjM} \right) dt. \tag{31}$$

where k_P and k_I are the proportional and integral coefficients, respectively.

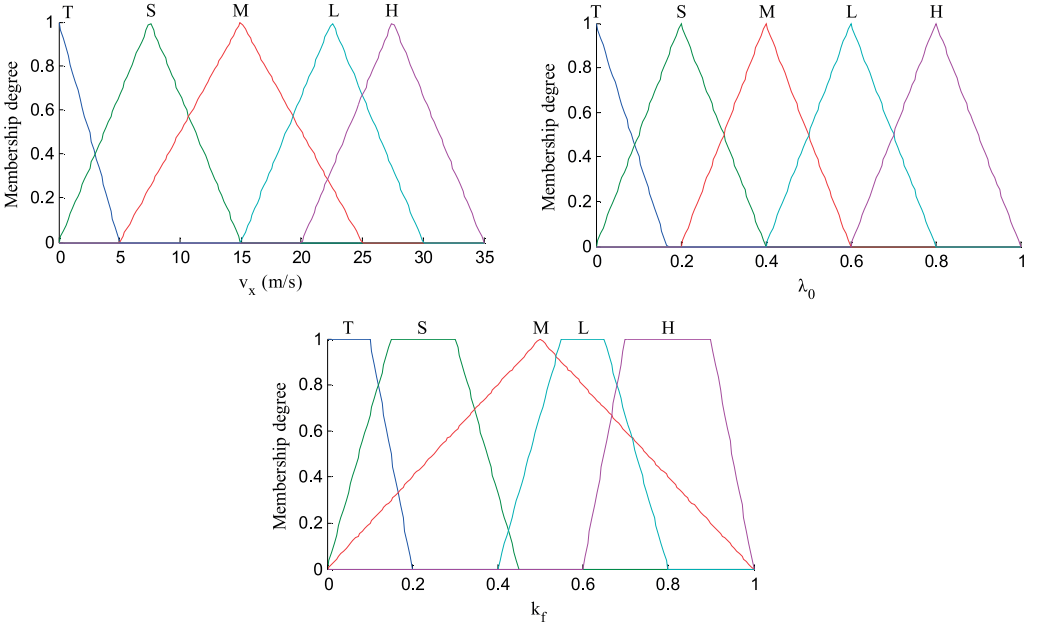

Fig. 5. Degree of membership functions of v_x, λ_0, and k_f.

Table 2. Fuzzy control rules.

k_m		λ_0				
		T	S	M	L	H
v_x	T	T	S	M	M	L
	S	T	S	M	L	L
	M	S	S	M	L	H
	L	H	M	L	H	H
	H	M	L	L	H	H

The calculated optimal longitudinal forces and lateral forces of the modified tire model are used as the inputs of RKF. In addition, v_x estimated by RKF is used to compute λ_0 and used as the input of fuzzy controller as a feedback. Thus, the overall estimation system forms a closed-loop feedback and iteration observer, the adaptive adjustment ability and anti-interference ability are enhanced, and the vehicle state estimation results are more accurate and reliable. At last, the vehicle sideslip angle is obtained by the estimation results of RKF and computed as $\beta = \arctan(v_y/v_x)$. The overall sideslip angle estimation strategy using cascaded multi-Kalman filters and the tire model modified in this paper is shown in Fig. 6.

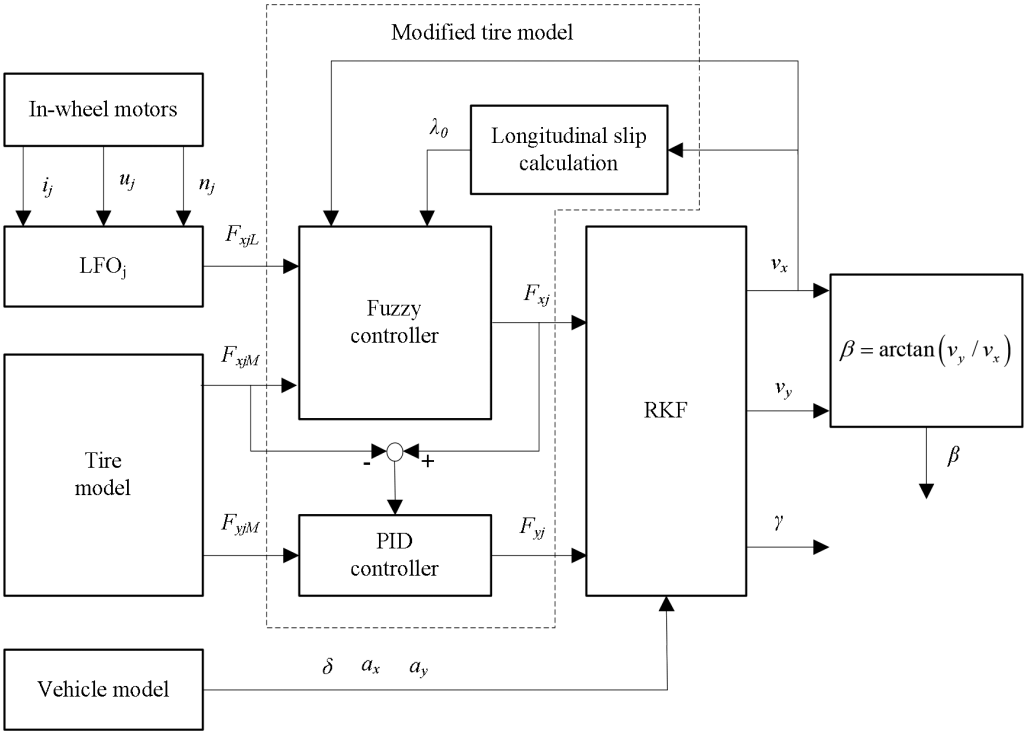

Fig. 6. The overall sideslip angle estimation strategy using cascaded multi-Kalman filters and the modified tire model.

4. Simulation results

In order to test effectiveness of the presented STF-based LFO and the RKF-based sideslip angle estimator presented in this paper, there were executed simulations using a high-fidelity CarSim-Simulink joint simulation platform. The CarSim software was used to provide the whole vehicle model; the LFOs and sideslip angle estimator were simulated in Matlab/Simulink. For further verification, the EKF-based LFO and EKF-based sideslip angle estimator were compared in the simulations with the STF-based LFO and the RKF-based sideslip angle estimator, respectively. The corresponding parameters of vehicle and in-wheel motors are listed in Table 3.

Table 3. Parameters of vehicle.

Symbol	Parameters	Value and units
m	Vehicle mass	710 kg
r	Effective radius of wheel	0.245 m
l_f	Distances from vehicle gravity center to the front axle	0.795 m
l_r	Distances from vehicle gravity center to the rear axle	0.975 m
b_f, b_r	Half treads of the front(rear) wheels	0.775 m
C_f	Equivalent cornering stiffness of front wheel	60000 N/rad
C_r	Equivalent cornering stiffness of rear wheel	40000 N/rad
I_z	Moment of inertia	1000 kg·m^2
R	Equivalent resistance of winding	0.688 Ω
K_a	Inverse electromotive force coefficient	0.06 Nm/A
K_t	Motor torque constant	11.43 Nm/A
J	Sum of inertia moment of wheel and motor	7.143 kg·m^2
b	Damping coefficient	0.643 Nm·sec/rad
L	Equivalent inductance of winding	0.125 H

4.1. S-turn manoeuvre

In this section, simulation of an S-turn manoeuvre is presented, in which the road friction coefficient is set to 0.8, the vehicle speed is maintained at a constant of 10 m/s, and the sine steering wheel angle is shown in Fig. 7. The LFOs are respectively designed for EDWM 1, 2, 3, 4, and in Fig. 8 their longitudinal force estimation results are compared. As shown in Fig. 8, both EKF-based LFO and STF-based LFO can estimate the longitudinal force accurately. In the local enlarged insets, it can be found that the estimation effect of STF is better than that of EKF. In the process of hand-steered wheel self-returning, the steering angle of hand wheel changes faster; there appears a fluctuation in the estimation results of longitudinal force. However, regarding the order of magnitude of longitudinal force, the fluctuation is relatively small, which indicates that the designed LFO can maintain good estimation performance when the state of the vehicle changes dramatically. As shown in Fig. 9 and Fig. 10, both EKF-based estimator and STF-based estimator can track the variation trend of vehicle state, but there exists an obvious deviation of the estimation results obtained by the EKF-based estimator. The deviation is caused by the uncertainty of vehicle model, and the RKF has a better stability for an unknown uncertainty. Moreover, the proposed sideslip angle estimation method using cascaded multi-Kalman filters and the modified tire model

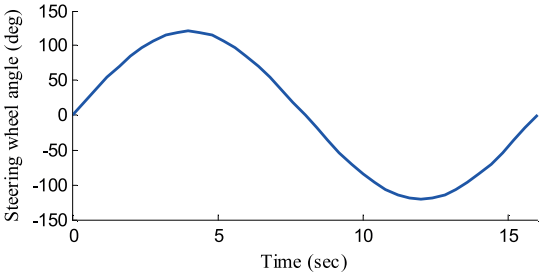

Fig. 7. Sine steering wheel angle.

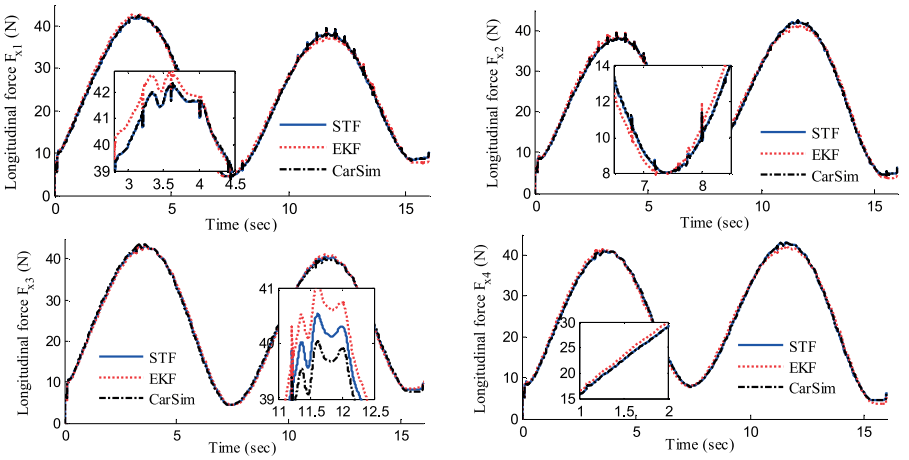

Fig. 8. Estimation of longitudinal forces in S-turn manoeuvre.

a) Longitudinal vehicle speed.

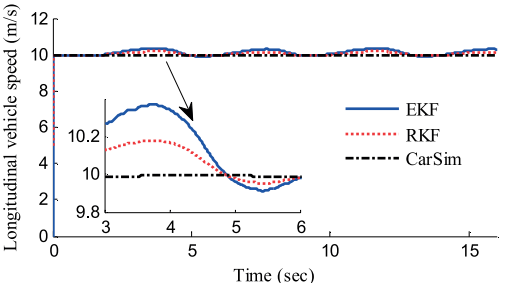

b) Lateral vehicle speed.

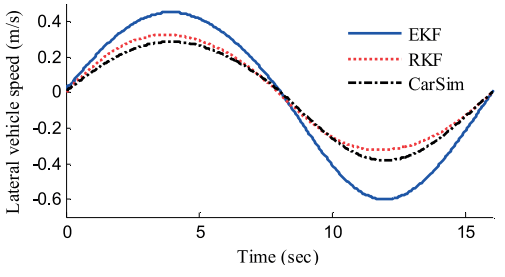

c) Yaw rate.

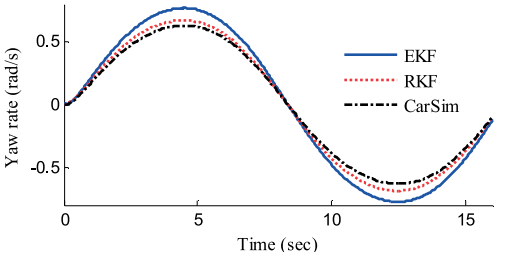

Fig. 9. Estimation of longitudinal vehicle speed, lateral vehicle speed and yaw rate in S-turn manoeuvre.

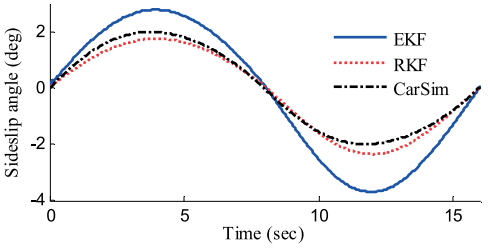

Fig. 10. Estimation of sideslip angle in S-turn manoeuvre.

has a high estimation accuracy and the estimation result is satisfactory. In order to further show the proposed estimation method's accuracy, the *root-mean-square* (RMS) error E_{RMS} between the real vehicle state and the estimated value is used for the quantitative evaluation and can be computed by the following equation:

$$E_{\mathrm{RMS}} = \sqrt{\frac{1}{N_s}\sum_{i=1}^{N_s}(x_i - x_{0i})^2}, \tag{32}$$

where N_s is the number of samples, x_1 and x_{0i} denote the estimated and measured vehicle state at the ith sample. Comparison of E_{RMS} values of vehicle state estimation in S-turn simulation is shown in Table 4. Notice that the presented method for longitudinal force, yaw rate and sideslip angle estimation improves the accuracy and reliability compared with the common estimation method.

Table 4. Comparison of E_{RMS} in S-turn manoeuvre.

E_{RMS}	Observer	
	EKF	**STF/RKF**
Longitudinal force F_{x1}	0.3854	0.1321
Longitudinal force F_{x2}	0.3014	0.1066
Longitudinal force F_{x3}	0.3773	0.1346
Longitudinal force F_{x4}	0.3111	0.1152
Longitudinal vehicle speed	0.2572	0.1248
Lateral vehicle speed	0.1892	0.0791
Yaw rate	0.0525	0.0219
Sideslip angle	0.1029	0.0304

4.2. Double Lane Changes manoeuvre

In this case, simulation of a *Double Lane Changes* (DLC) manoeuvre, as shown in Fig. 11, is carried out. In the simulation, the road friction coefficient is set to 1.0. The vehicle speed is maintained at a constant of 25 m/s. Fig. 12 presents comparison of the longitudinal force estimation results. Like the estimation results of S-turn manoeuvre simulation, the estimation results of EKF-based and STF-based estimators are satisfactory, but the STF has a more accurate following ability. As it is shown in Fig. 13 and Fig. 14, with the influence of model uncertainty, the RKF-based estimator has better performance in dealing with uncertainty interference compared

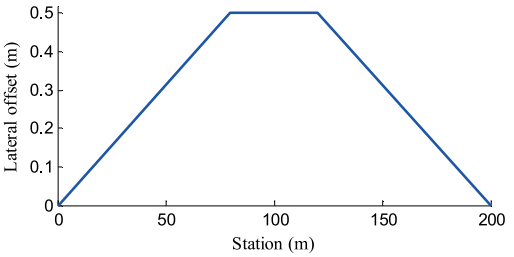

Fig. 11. DLC manoeuvre.

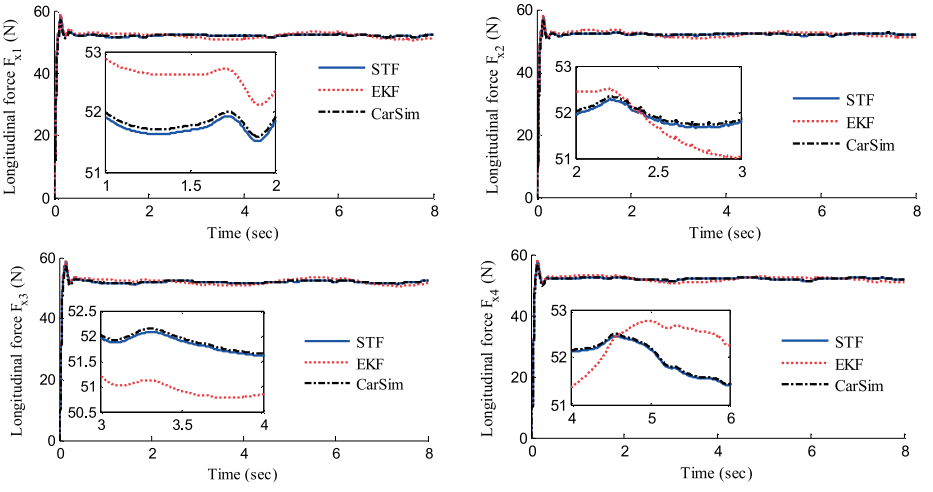

Fig. 12. Estimation of longitudinal forces in DLC manoeuvre.

with EKF, however, the estimation results of EKF-based estimator have some deviations when the steering angle of hand wheel is relatively large. And the presented modified tire model contributes to improvement of the sideslip angle estimation accuracy. Analogously to the processing method in S-turn simulation, the E_{RMS} values of DLC simulation are calculated and listed is Table 5. Thus, effectiveness of the proposed estimation method is verified.

Table 5. Comparison of E_{RMS} in DLC manoeuvre.

E_{RMS}	Observer	
	EKF	**STF/RKF**
Longitudinal force F_{x1}	0.7384	0.3055
Longitudinal force F_{x2}	0.7736	0.3267
Longitudinal force F_{x3}	0.7601	0.3123
Longitudinal force F_{x4}	0.7465	0.3259
Longitudinal vehicle speed	0.3346	0.2815
Lateral vehicle speed	0.2013	0.1176
Yaw rate	0.1725	0.0615
Sideslip angle	0.1304	0.0767

a) Longitudinal vehicle speed.

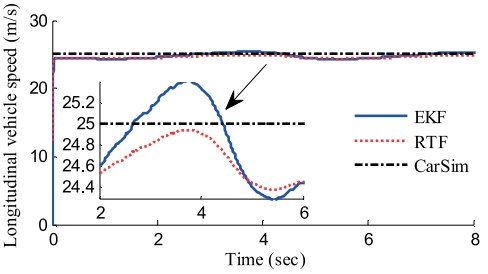

b) Lateral vehicle speed.

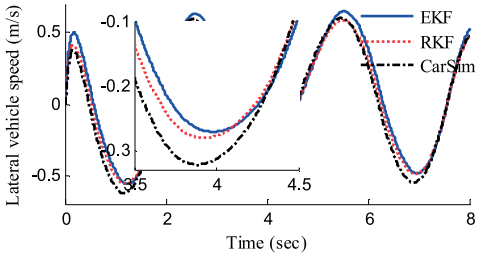

c) Yaw rate.

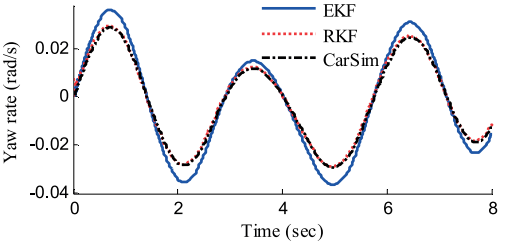

Fig. 13. Estimation of longitudinal vehicle speed, lateral vehicle speed and yaw rate in DLC manoeuvre.

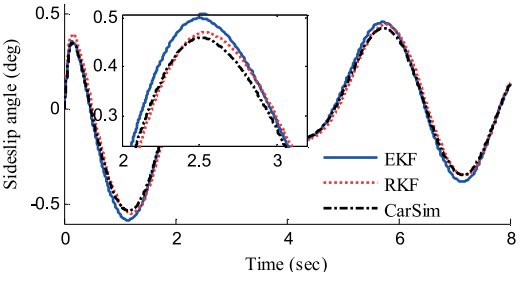

Fig. 14. Estimation of sideslip angle in DLC manoeuvre.

5. Experimental results

5.1. Experimental vehicle

In this section, there is presented an experiment for practical validation of the proposed estimation method performance. Considering that the sensors for longitudinal force measurements

are still unavailable on board our four-wheel independent-drive electric vehicle, the verification of LFO is achieved by an experiment on a chassis dynamometer bench. The RKF-based estimator is validated by the experimental data of road test, in which the longitudinal forces estimated by LFOs are used as the credible pseudo-measurements of RKF.

The vehicle for bench test and road test is a four-wheel independent-drive electric vehicle which is refitted from a single-motor drive electric vehicle and actuated by four in-wheel motors, and the mass, rated power, maximum torque and maximum speed of each in-wheel motor are 18.6 kg, 3 KW, 150 Nm and 750 r/min, respectively. The vehicle power source is a lithium iron phosphate battery pack with 72 V voltage output and 140 Ah battery rated capacity, and the vehicle control system is powered by a 12 V power supply transformed by a DC/DC converter. The whole vehicle control system is built on a *rapid prototyping platform* (RPP), which is used for development of a model-based control system. The signals measured with the sensors RPP is equipped with, are utilized as the control input of RPP. At the same time, the RPP is used to automatically design a control algorithm for electromechanical actuators and to implement it simultaneously into a target microprocessor. The control network framework of the modified four-wheel independent-drive electric vehicle is shown in Fig. 15.

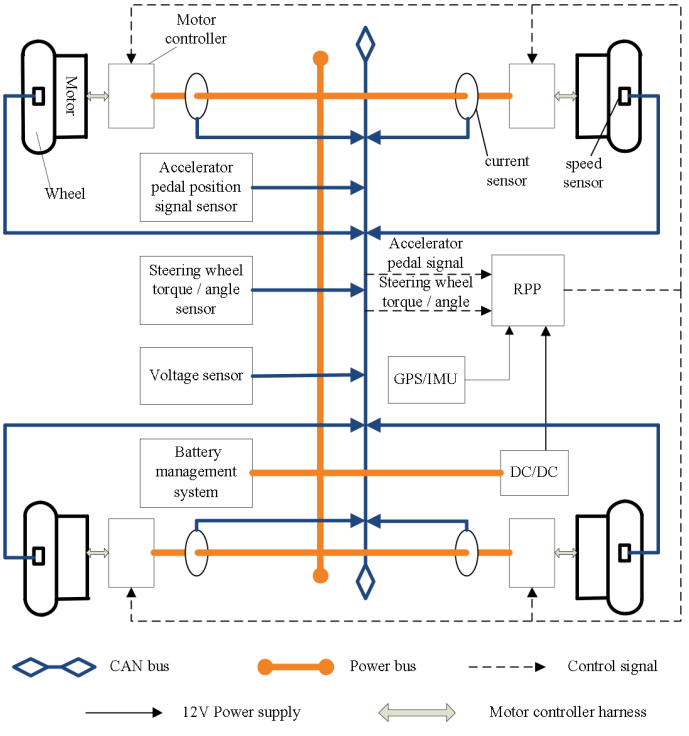

Fig. 15. The control network framework of the experimental 4WID-EV.

Figure 16 shows the overall-vehicle signal transmission system based on RPP. All control signals and sensor signals are transferred by a CAN bus. The data from the vehicle sensors and corresponding vehicle control signals are acquired in the form of analogue quantity and frequency quantity. Then, the PWM output channel is used to interpret the control signals for each in-wheel

motor controller through real-time analysis and processing of the sensor data. Considering that the control signals of in-wheel motor controllers are analogue, the D/A converters are designed and used to achieve an extra transformation of control signals in order to make them compatible with those of motor controllers, so that the I/O matching between the motor controller and RPP is achieved. Using the CAN bus of RPP, the sensor signals and control signals are recorded by CAN tools of Vehicle SPY 3.

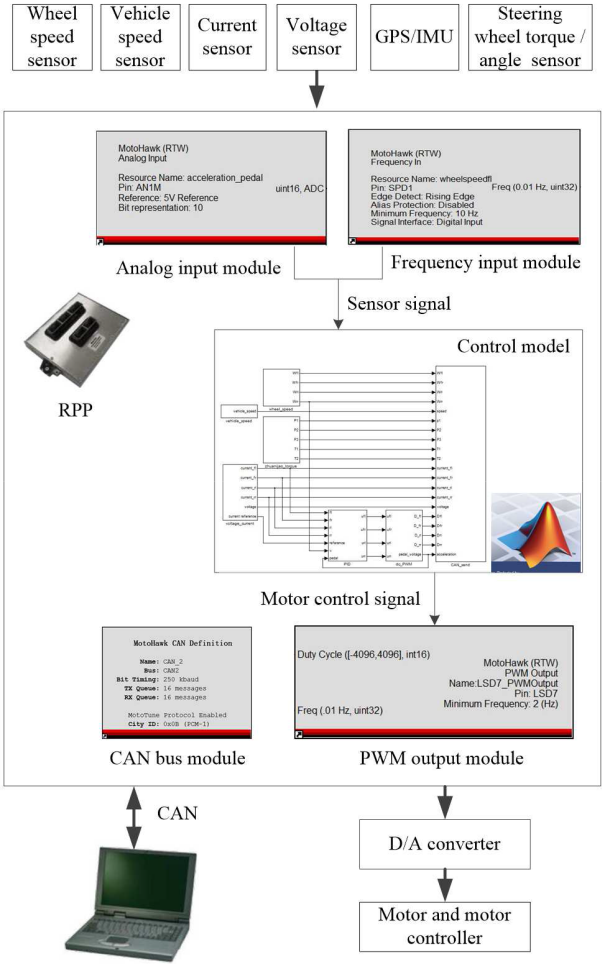

Fig. 16. The overall-vehicle signal transmission system based on RPP.

5.2. Test on chassis dynamometer bench

Figure 17 shows the chassis dynamometer bench for vehicle test. The vehicle for test was a four-wheel independent-drive electric vehicle which was refitted from a single-motor drive electric vehicle and actuated by four in-wheel motors. The whole vehicle control system was built on a rapid prototyping platform. The current, speed and voltage values of in-wheel motors were measured with corresponding sensors and recorded by the host computer via the CAN bus.

The longitudinal forces were recorded by the data acquisition system of chassis dynamometer. Here, the experimental data of front-right electric-driven wheel were chosen to verify the designed LFO, and the estimation results are shown in Fig. 18. As we can see, in the process of vehicle acceleration, the STF-based LFO has higher estimation accuracy. When the vehicle tends to travel at a uniform speed, the estimation results of STF-based LFO tend to converge faster. It indicates that the real-time estimation ability of the STF-based LFO is better than that of the EKF-based estimator, and the estimation performance in practice is verified.

Fig. 17. A vehicle test on a chassis dynamometer bench.

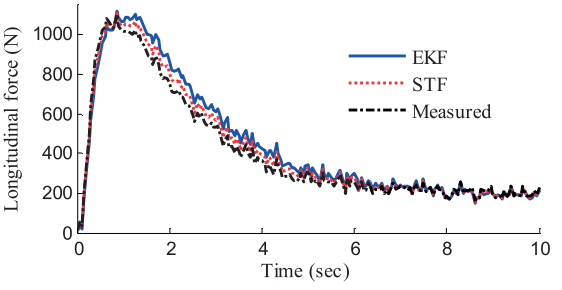

Fig. 18. Estimation of longitudinal forces.

5.3. Road test

Figure 19a shows a photo of the vehicle road test. As shown in Fig. 19b, the road test is implemented in the form of a slalom trajectory, in which 10 traffic piles are placed as obstacles, and the distance between every two adjacent piles is 30 meters. The vehicle speed cruising is well regulated by a designed speed controller in RPP. Fig. 19c and Fig. 19d show the measurement results of steering wheel angle and vehicle speed in the road test, respectively. The front wheel steering angle was transformed from the measured hand-steered wheel angle. The longitudinal vehicle speed and sideslip angle were measured by a high-precision difference *global position system* (GPS), and the yaw rate was obtained from an *inertial measurement unit* (IMU). Fig. 20 and Fig. 21 present the estimation results of EKF-based and RKF-based estimators. Through comparative analyses, it can be found that the real-time tracking ability and estimation accuracy of the proposed estimation method is superior to those obtained with common EKF-based methods.

Although the error of experimental results is slightly larger than that of simulation results, the error is still within the allowable range. Comparison of E_{RMS} values in the chassis dynamometer bench test and the road test is shown in Table 6, and the feasibility in practice of the estimation method proposed in this paper is further validated.

a) The experimental vehicle.

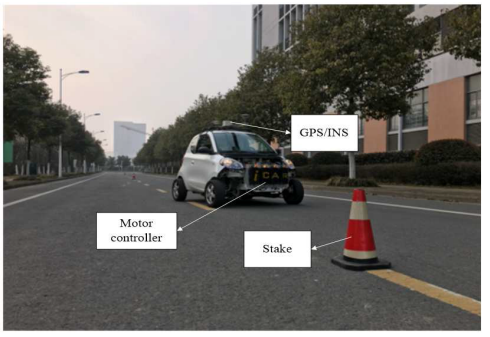

b) Experimental trajectory.

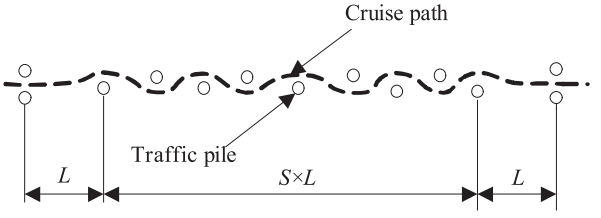

c) Steering wheel angle.

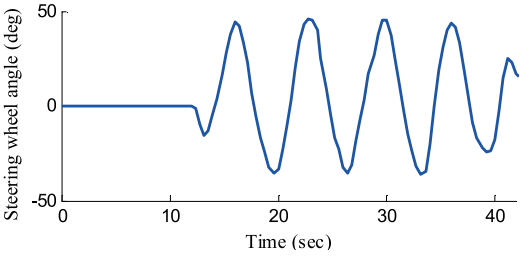

d) Vehicle speed.

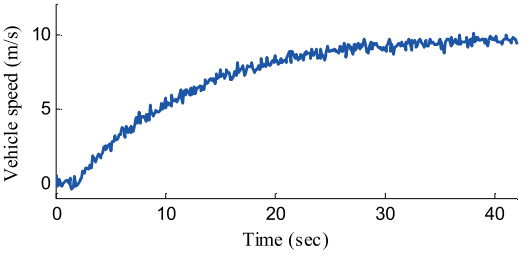

Fig. 19. The road test.

a) Longitudinal vehicle speed.

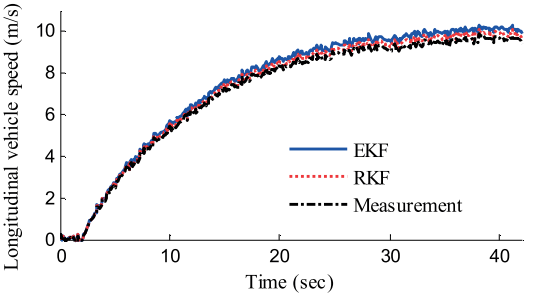

b) Lateral vehicle speed.

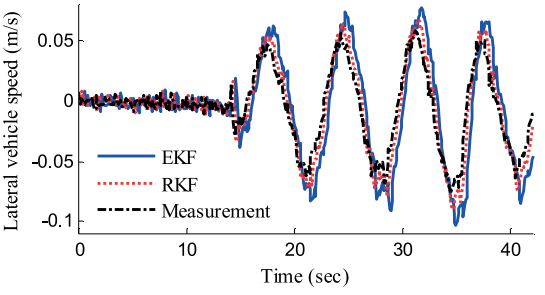

c) Yaw rate.

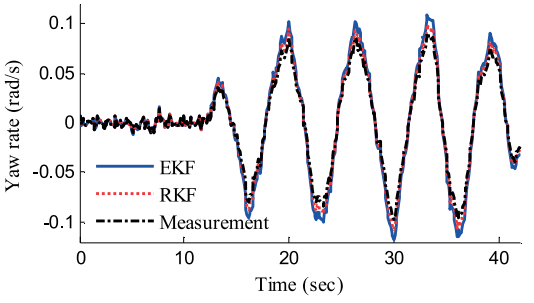

Fig. 20. Estimation of longitudinal vehicle speed, lateral vehicle speed and yaw rate in the road test.

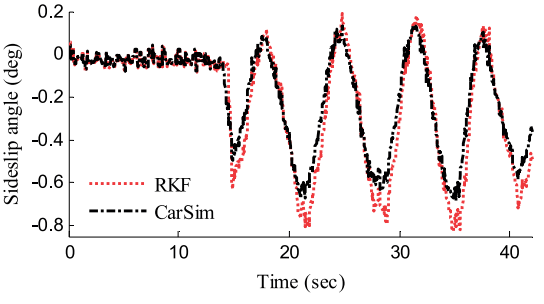

Fig. 21. Estimation of sideslip angle in the road test.

Table 6. Comparison of E_{RMS} in the experiment.

E_{RMS}	Observer	
	EKF	**STF/RKF**
Longitudinal force	1.1044	0.6976
Longitudinal vehicle speed	0.1764	0.1002
Lateral vehicle speed	0.1388	0.0893
Yaw rate	0.1107	0.0723
Sideslip angle	0.1121	0.0814

6. Conclusion

This paper presents a novel STF-based LFO and an RKF-based sideslip angle estimator for 4WID-EVs with a modified tire model being applied to improve the accuracy of sideslip angle estimation. Owing to the longitudinal force that is the unknown input of EDWM, we expanded the system of EDWM and structured the differential equation of longitudinal force, and then designed the LFO based on STF. Considering the model uncertainty, the sideslip angle estimation was achieved with the design of RKF. Moreover, a novel modified tire model was proposed to enhance the reliability and accuracy of the estimation system by iteration of information and fusion of the multi-Kalman filters. Simulations of S-turn and DLC manoeuvres were carried out, the simulation results verified effectiveness of the presented LFO, and it can be deduced that the RKF-based sideslip angle estimator improves the accuracy and reliability of estimation with the variation of tire cornering stiffness. For further validation, a test on a chassis dynamometer bench and a road test were performed, and performance of the proposed estimation method was validated.

Acknowledgements

This work was supported by the National Natural Science Foundation of China (grant numbers U1564201 and U1664258), National Key Research and Development Program of China (grant number 2017YFB0102603), Key R&D Plan of Jiangsu Province (grant number BE 2016149 and BE2017129), 333 Project of Jiangsu Province (grant numberBRA2016445), Natural Science Foundation of Jiangsu Province (grant number BK 20160525), and Natural Science Foundation of colleges and universities in Jiangsu Province (grant number 16KJB580012).

References

[1] Wang, R,R., Zhang, H., Wang, J.M. (2014). Linear parameter-varying controller design for four wheel independently-actuated electric ground vehicles with active steering systems. *IEEE Trans. Control. Syst. Technol.*, 22(4), 1281–1296.

[2] Guo, J.G., Dong H.X., Sheng, W.H., Tu, C. (2018). Optimum control strategy of regenerative braking energy for electric vehicle. *Journal of Jiangsu University: Natural Science Editions*, 39(2), 132–138.

[3] Chen, T., Xu, X., Chen, L., Jiang, H.B., Cai, Y.F. (2018). Estimation of longitudinal force, lateral vehicle speed and yaw rate for four-wheel independent driven electric vehicles. *Mech. Syst. Signal Process*, 101, 377–388.

[4] Shuai, Z.B., Zhang, H., Wang, J.M., Li, J.Q., Ouyang, M.G. (2014). Combined AFS and DYC control of four-wheel-independent-drive electric vehicles over CAN Network with time-varying delays. *IEEE Trans. Veh. Technol.*, 63(2), 591–602.

[5] Zhang, H., Wang, J.M. (2017). Active steering actuator fault detection for an automatically-steered electric ground vehicle. *IEEE Trans. Veh. Technol.*, 66(5), 3685–3702.

[6] Jin, X.J., Yin, G.D., Chen, N. (2015). Gain-scheduled robust control for lateral stability of four-wheel-independent-drive electric vehicles via linear parameter-varying technique. *Mechatronics*, 30, 286–296.

[7] Wang, R.R., Zhang, H., Wang, J.M., Yan, F.J., Chen, N. (2015). Robust lateral motion control of four-wheel independently actuated electric vehicles with tire force saturation consideration. *Journal of The Franklin Institute*, 352, 645–668.

[8] Nam, K., Fujimoto, H., Hori, Y. (2012). Lateral stability control of in-wheel-motor-driven electric vehicles based on sideslip angle estimation using lateral tire force sensors. *IEEE Trans. Veh. Technol.*, 61(5), 1972–1985.

[9] Xu, X., Chen, T., Chen, L., Wang, W.J. (2016). Longitudinal force estimation for motorized wheels driving electric vehicle based on improved closed-loop subspace identification. *Journal of Jiangsu University: Natural Science Editions*, 37(6), 650–656.

[10] Zhang, H., Zhang, G.G., Wang, J.M. (2016). H∞ observer design for LPV systems with uncertain measurements on scheduling variables: application to an electric ground vehicle. *IEEE/ASME Trans. Mechatronics*, 21(3), 1659–1670.

[11] Wang, R.R., Jing, H., Hu, C., Yan, F.J., Chen, N. (2016). Robust H∞ path following control for autonomous ground vehicles with delay and date dropout. *IEEE Trans. Intell. Transp. Syst.*, 17(7), 2042–2049.

[12] Hu, C., Wang, R.R., Yan, F.J., Chen, N. (2016). Output constraint control on path following of four-wheel independently actuated autonomous ground vehicles. *IEEE Trans. Veh. Technol.*, 65(6), 4033-4043.

[13] Wang, R.R., Hu, C., Yan, F.J., Chadli, M. (2016). Composite nonlinear feedback control for path following of four-wheel independently actuated autonomous ground vehicles. *IEEE Trans. Intell. Transp. Syst.*, 17(7), 2063–2074.

[14] Jiang H.B., Cao, F.G., Zhu, W.W. (2018). Control method of intelligent vehicles cluster motion based on SMC. *Journal of Jiangsu University: Natural Science Editions*, 39(4), 385–390.

[15] Chen, B., Hsieh, F. (2008). Sideslip angle estimation using extended Kalman filter. *Vehicle Syst. Dyn.*, 46(1), 353–364.

[16] Li, L., Song, J., Li, H.Z., Zhang, X.L. (2011). A variable structure adaptive extended Kalman filter for vehicle slip angle estimation. *Int. J. Veh. Des.*, 56(1–4), 161–185.

[17] Boada, B.L., Boada, M.J.L., Diaz, V. (2016). Vehicle side slip angle measurement based on sensor data fusion using an integrated ANFIS and an Unscented Kalman Filter algorithm. *Mech. Syst. Signal Process.*, 72, 832–845.

[18] Li, L., Jia, G., Ran, X., Song, J., Wu, K.H. (2014). Avariable structure extended Kalman filter for vehicle side slip angle estimation on a low friction road. *Veh. Syst. Dyn.*, 52(2), 280–308.

[19] Liu, Y.H., Li, T., Yang, Y.Y., Ji, X.W., Wu, J. (2017). Estimation of tire-road friction coefficient based on combined APF-IEKF and iteration algorithm. *Mech. Syst. Signal Process.*, 88, 25–35.

[20] Leung, K.T., Whildborne, J.F., Purdy, D., Dunoyer, A. (2011). A review of ground vehicle dynamic state estimations utilising GPS/INS. *Vehicle Syst. Dyn.*, 49(1–2), 29–58.

[21] Nam, K., Oh, S., Fujimoto, H. Hori, Y. (2013). Estimation of sideslip angle and roll angles of electric vehicles using lateral tire force sensors through RLS and Kalman filter approaches. *IEEE Trans. Ind. Electron.*, 60(3), 988–1000.

[22] Ma, B., Liu, Y.H., Gao, Y.F., Yang, Y.Y., Ji, X.W., Bo, Y. (2018). Estimation of vehicle sideslip angle based on steering torque. *Int. J. Adv. Manuf. Technol.*, 94(9–12), 3229–3237.

[23] Liu, W., He, H.W., Sun, F.C. (2016). Vehicle state estimation based on minimum model error criterion combining with extended Kalman filter. *Journal of The Franklin Institute*, 353, 834–856.

[24] Jin, X.J., Yin, G.D. (2015). Estimation of lateral tire-road forces and sideslip angle for electric vehicles using interacting multiple model filter approach. *Journal of The Franklin Institute*, 352, 686–707.

[25] Leung, K.T., Whildborne, J.F., Purdy, D., Barber P. (2011). Road vehicle state estimation using low-cost GPS/INS. *Mech. Syst. Signal Process.*, 25(6), 1988–2004.

[26] Bevly, D.M., Ryu, J.H., Gerdes, J.C. (2006). Integrating INS sensors with GPS measurements for continuous estimation of vehicle sideslip, roll, and tire cornering stiffness. *IEEE Trans. Intell. Transport. Syst.*, 7(4), 483–493.

[27] Damrongrit, P., Rajesh, R., John, A.G., Lew, J.Y. (2009). Development and experimental evaluation of a slip angle estimator for vehicle stability control. *IEEE Trans. Control Syst. Technol.*, 17(1), 78–88.

[28] Tuononen, A.J. (2009). Vehicle lateral state estimation based on measured tyre forces. *Sensors*, 9, 8761–8775.

[29] Yoon, J.H., Li, S.E., Ahn C. (2016). Estimation of vehicle sideslip angle and tire-road friction coefficient based on magnetometer with GPS. *Int. J. Automotive Technology*, 17(3), 427–435.

[30] Madhusudhanan, A.K., Corno, M., Holweg, E. (2016). Vehicle sideslip estimator using load sensing bearings. *Control Eng. Pract.*, 54, 46–57.

[31] Yoon, J.H., Peng, H. A cost-effective sideslip estimation method using velocity measurements from two GPS receivers. *IEEE Trans. Veh. Technol.*, 63(6), 2589–2599.

[32] Wang, R., Wang, J.M. (2013). Tire-road friction coefficient and tire cornering stiffness estimation based on longitudinal tire force difference generation. *Control Eng. Pract.*, 21(1), 65–75.

[33] Chen, L., Bian, M., Luo, Y.G., Li, K.Q. (2015). Real-time identification of the tyre-road friction coefficient using an unscented Kalman filter and mean-square-error-weighted fusion. *Proc. Inst. Mech. Eng. D. J. Automob. Eng.*, 230(6), 788–802

[34] Li, X., Song, X, Chan CY. (2014). Reliable vehicle sideslip angle fusion estimation using low-cost sensors. *Measurement*, 51, 241–258.

[35] Zhang, H., Huang, X.Y., Wang, J.M., Karimi, H.R. (2015). Robust energy-to-peak sideslip angle estimation with applications to ground vehicles. *Mechatronics*, 30, 338–347.

[36] Yoon, J.H., Peng, H. (2014). Robust vehicle sideslip angle estimation through a disturbance rejection filter that integrates a magnetometer with GPS. *IEEE Trans. Intell. Transp. Syst.*, 15(1), 191–204.

[37] Wang, R.R,, Hu, C., Wang, Z.J., Yan, F.J., Chen, N. (2015). Integrated optimal dynamics control of 4WD4WS electric ground vehicle with tire-road frictional coefficient estimation. *Mech. Syst. Signal Process*, 60–61, 727–741.